# Dual-wavelength hybrid Tamm plasmonic laser

SHAHED-E-ZUMRAT,[1,2] ⓘ SHADMAN SHAHID,[1,2] ⓘ AND MUHAMMAD ANISUZZAMAN TALUKDER[1,*] ⓘ

[1]*Department of Electrical and Electronic Engineering, Bangladesh University of Engineering and Technology, Dhaka 1205, Bangladesh*
[2]*Co-first authors with equal contribution*
*anis@eee.buet.ac.bd*

**Abstract:** Miniature lasers emitting dual-wavelength modes have diverse applications alongside the more explored single-mode counterparts. However, having dual-wavelength modes originating from a plasmonic-photonic hybrid laser is still a relatively new area for research. Compared to the amount of literature devoted to the physics of such hybrid cavities, only a few have analyzed their role in lasing applications. Notably, the role of hybrid cavities in dual-wavelength lasing is still unexplored. In this work, the properties of one-dimensional distributed Bragg reflectors and thin metal nanohole arrays come together to create a hybrid dual-mode plasmonic laser. The similar energy distribution characteristics of photonic and plasmonic lasers make hybrid structures a viable choice for efficient dual-mode lasing. In this work, the lasing cavity simultaneously excites photonic and Tamm plasmonic modes to generate dual-mode lasing. Consequently, the proposed laser shows high emission output with narrow linewidth and a clear and tunable mode separation.

## 1. Introduction

In photonics research, there has been an increasing interest in integrating photonic and plasmonic components with on-chip electronics [1–3]. In this regard, scaled-down lasers are essential as an optical source in photonic integrated circuits (PICs). In PICs, wavelength multiplexing can significantly increase integration density where space and energy availability are constrained. Therefore, wavelength multiplexing is a prime application area for dual-wavelength lasers. Additionally, dual-wavelength lasers are required for on-chip optical interconnects, remote sensing for multiple target substances simultaneously, microwave communications, terahertz difference frequency generation, and distance measurements using the two-wavelength interferometry [4–11]. Furthermore, a dual-mode laser is convenient when space is a constraint in integrated circuits to avoid using two separate lasers.

Metallic nanostructures are often exploited to miniaturize laser cavity dimensions [12,13]. Since the seminal paper by Bergman et al. in 2003, reporting the theory for the first time behind surface plasmon amplification through stimulated emission of radiation via metal nanoparticles [14], plasmonic lasers have come a long way. To date, various cavity topologies and designs have led to a wide variety of plasmonic lasers [15]. Recently, metallic nanoparticle arrays or nanohole arrays (NHAs) have been introduced in plasmonic lasers to address the weak solitary feedback, lack of directionality, and high losses of single-particle plasmonic lasers [16–19]. Nevertheless, despite offering improved mode confinement, the ohmic loss associated with metals leads to a low quality factor ($Q$) in plasmonic nanocavities.

In contrast, traditional dielectric cavities exhibit ultra-high $Q$ [20,21]. Therefore, hybridizing plasmonic effects with their photonic counterparts can be a suitable workaround to overcome these challenges and develop a high-$Q$ cavity with improved mode confinement [22]. Tamm plasmon (TP) mode is one such hybrid plasmonic mode that offers higher $Q$ than the surface plasmon polariton (SPP) modes [22–24]. TP mode arises due to the coupling of the photon and plasmon resonance at the interface between a one-dimensional (1D) photonic crystal and

metal. Furthermore, TP modes can be hybridized with photonic modes to control the spectral position, intensity of the resonance, and the number of resonant modes in a cavity. Multiple topologies have been delved into exploiting the capabilities offered by hybridizing TP resonances. Hybrid modes occur when TPs are coupled with other resonances, such as photonic cavity modes [25–28], exciton polaritons [29], SPPs [30] and LSPs [31]. The capability of hybridization has made TPs a prospective tool that can be exploited in various fields of application, such as lasers, where the energy coupled from the TP mode will provide stimulated feedback for lasing action.

To date, only a few cavity plasmonic resonance-based topologies have been proposed to achieve dual or multiple cavity modes [32–34]. Wang et al. reported the first multimode plasmonic laser, incorporating a metal-nanoparticle-superlattice structure [32]. Later in 2019, Pourjamal et al. reported dual-mode plasmonic lasing in nickel-nanodisk arrays [33]. The following year, a quantum-dot plasmonic lattice laser was reported to exhibit dual-mode emission by Winkler et al. [34]. However, the designs of these previous works either utilize a larger device area to generate a dual-mode emission [32] or different periodicities along the *x*- and *y*-directions, resulting in a broader divergence angle. In addition, these devices are also significantly affected by the typical drawbacks of a plasmonic system, i.e., ohmic losses in metals, leading to a higher threshold and a more significant loss in the emitted beam. Therefore, there is still a need to create a dual-mode laser that will localize emission in the nanoscale range, consume low power and have a high-$Q$ mode with minimal divergence.

Recently, we reported a planar multi-layer plasmonic laser structure exhibiting dual-mode lasing due to a merged lattice patterning of the metal layer [35]. This laser showed an ultra-low threshold but with a substantial overlap of the lasing modes and the output sensitively depending on the merged lattice dimensional parameters. In contrast, this work presents a dual-mode plasmonic laser consisting of two distributed Bragg reflectors (DBRs) terminated by a perforated metal film. The topology of the proposed device is $DBR_1$–gain medium–$DBR_2$–metal NHA. This topology has a similarity with the DBR–active medium–DBR structure of vertical-cavity surface-emitting lasers (VCSEL). The proposed laser cavity will help excite photonic modes in addition to plasmonic modes with the potential for minimizing losses and wider separations between the lasing modes. The multi-layer dielectric stacks are also easier to fabricate than creating complex merged-lattice patterns onto a gold film, as used in Ref. [35].

Recently, a laser structurally similar to VCSELs has been reported by Liu et al. for dual-wavelength lasing at the terahertz frequency range, where DBRs have been employed on both sides of the active medium [36]. Two DBRs on the sides of the active medium act as mirrors, creating an optical cavity and providing feedback. In contrast, this work shows that photonic modes between two DBRs and TP modes between $DBR_2$ and metal interact and generate a dual-wavelength lasing spectrum. The modes of such a structure have high $Q$ and small volume [37]. Also, the deployment of DBRs overcomes the ohmic losses of the plasmonic laser by selectively amplifying the lasing emission. The metal layer is thin enough to ensure that the lasing emission is effectively transmitted through the metal-NHA film via an extraordinary optical transmission (EOT). The spectral positions of the hybrid modes depend on the metal layer's thickness, material, and patterning and the properties of the neighboring dielectric layers of the DBRs. In cavity design, coupling the TP and photonic modes offers the required resonance for laser cavity design. This work further analyzes the two modes and finds that each is distinct, and their origins are traced back to the respective TP and photonic modes. Also, the emission wavelengths of the proposed dual-mode laser are tunable over a broad range, rendering it useful for various applications.

This paper is ordered as follows: Section 2 introduces the designed plasmonic laser structure. Section 3 explains the numerical modeling and methodology of the work. Section 4 presents the characteristics of the passive lasing cavity through a physical and functional evolution of the

structure leading up to the analysis of the plasmonic laser itself. Finally, Sec. 5 summarizes the findings and offers concluding insights.

## 2. Proposed device configuration

Figure 1 shows the schematic illustration of the proposed dual-mode laser structure. The gain medium of the proposed laser structure is placed between two DBRs. At the far end of the device, i.e., opposite to the pumping side, there is a thin planar gold (Au) layer, perforated with an array of 100 nm × 100 nm square nanoholes. The spacing between the adjacent nanoholes, i.e., periodicity ($\Lambda$), is 275 nm in both the $y$- and $z$-directions. The gain medium is a 325-nm-thick slab, denoted as $d_M$, consisting of IR-140 dye molecules embedded in a polyurethane (PU) matrix. Both DBRs, hereafter referred to as $DBR_1$ and $DBR_2$, comprise alternating layers of non-dispersive $TiO_2$ and $MgF_2$, as shown in Fig. 1(a). $DBR_1$ is composed of seven $TiO_2$–$MgF_2$ pairs, while $DBR_2$ is composed of eight such pairs. Following $DBR_2$, there is a terminating $TiO_2$ layer with a thickness ($d_L$) of 210 nm. A perforated NHA Au film of 100-nm thickness follows the $TiO_2$ layer. The optical property of Au is modeled following Ref. [38]. The terminating $TiO_2$ layer is used for tuning the lasing wavelength. $TiO_2$ and $MgF_2$ layers have refractive indices of 2.23 and 1.46, respectively [39]. The optical pump has been modeled assuming a plane wave source emitting a 40-fs pulse at the 375-THz frequency and placed at the far end of $DBR_1$.
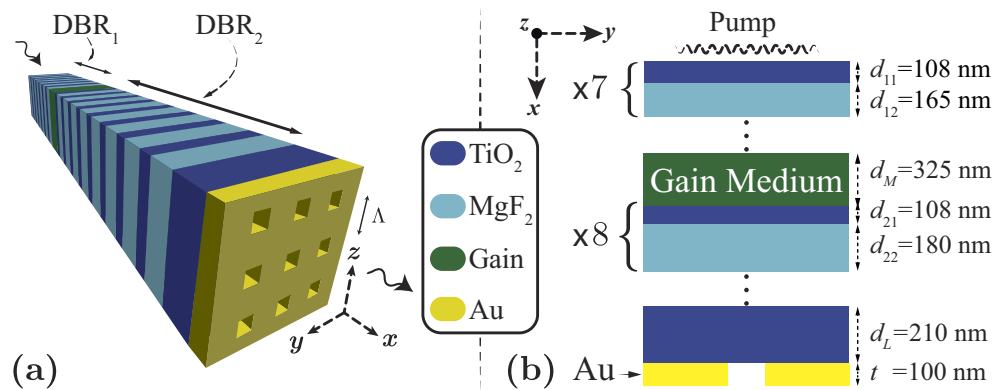


**Fig. 1.** (a) Three-dimensional (3D) schematic view of the proposed laser structure. (b) Longitudinal cross-sectional view of the proposed laser structure. Here, hole-to-hole distance in the Au-film, $\Lambda$ = 275 nm.

## 3. Mathematical model and simulation methodology

The interactions of the plasmonic laser structure with the incident pump pulse and subsequent lasing have been simulated by solving Maxwell's equations using the finite-difference time-domain (FDTD) technique [40]. FDTD simulations have been performed using Lumerical [41]. The IR-140 dye molecule-embedded PU gain medium used in the laser structure is modeled as a four-level two-electron atomic system, as schematically shown in Fig. 2 [42,43]. The model abides by Pauli's exclusion principle and follows the rate equation formulation presented in Ref. [43]. Here, electrons are optically pumped from level 0 to 3. Lasing emission occurs for stimulated electron transitions from level 2 to 1. Transitions from levels 3 to 2 and 1 to 0 are non-radiative and very rapid. The PU host material for dye molecules has an index of 1.51 [18]. The different parameter values of the gain medium are obtained from Refs. [18] and [44] and tabulated in the table in Fig. 2(b).
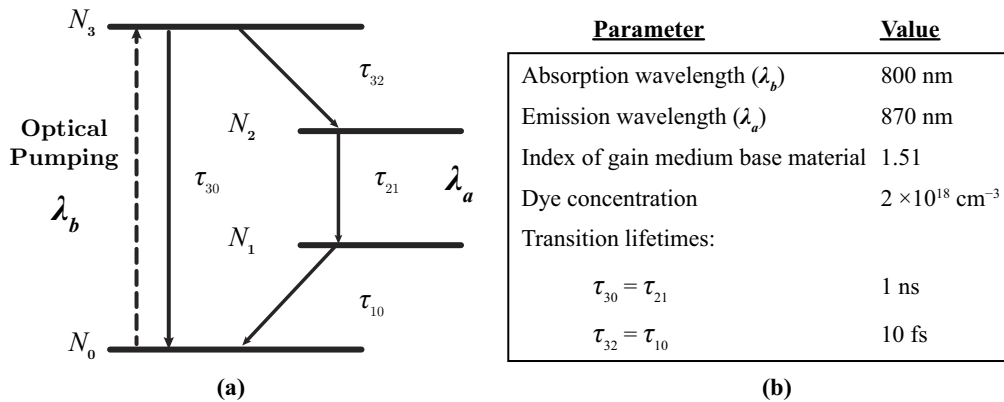
| Parameter | Value |
|---|---|
| Absorption wavelength ($\lambda_b$) | 800 nm |
| Emission wavelength ($\lambda_a$) | 870 nm |
| Index of gain medium base material | 1.51 |
| Dye concentration | $2 \times 10^{18}$ cm$^{-3}$ |
| Transition lifetimes: | |
| $\tau_{30} = \tau_{21}$ | 1 ns |
| $\tau_{32} = \tau_{10}$ | 10 fs |

(a)                                                              (b)

**Fig. 2.** (a) Four-level two-electron model of the gain medium. (b) Parameter values of the four-level two-electron gain medium model of the IR-140 dye used in simulation.

The pump pulse energy is resonant with the energy gap between levels 0 and 3 of IR-140 molecules. The pump pulse is incident along the *x*-direction, as shown in Fig. 1, with the electric field oscillating along the *z*-direction. Since the structure is periodic along the *y*- and *z*-directions, the simulation region has been delimited by the unit cell dimensions along the *y*- and *z*-directions using the Bloch boundary conditions. Perfectly matched layers (PML) boundary conditions have been used along the direction of wave propagation, i.e., *x*-direction.

## 4.    Results and discussion

The characteristic plasmonic and photonic modes associated with the proposed laser cavity will determine the lasing emission modes. Hence, this work analyzes the proposed cavity's transmission and reflection characteristics to understand and explain the lasing emission spectra. In addition, the modes excited within the lasing cavity have been investigated step-by-step by decomposing the proposed structure into constituent components.

### 4.1.    Cavity mechanism

The proposed laser cavity consists of a 1D dielectric heterostructure, DBR$_1$–PU–DBR$_2$, terminated by a thin metal layer perforated with an NHA. The modes formed by the dielectric heterostructure and metal layer propagate through the NHA via EOT. The proposed structure has been designed to support two hybrid spectral modes created by the coupling of plasmonic and photonic modes. The TP mode is excited at the metal–dielectric interface, while the photonic mode is excited between the DBRs. The photonic mode exhibits a high *Q* and ensures efficient absorption of photons within the gain medium, overcoming the characteristic losses to metals in a plasmonic mode [22]. However, the TP mode exhibits the advantageous properties of plasmons, such as good confinement and low mode volume [45] but incurs ohmic losses associated with metals [14,46]. When the plasmonic and photonic modes are simultaneously excited within the cavity, they interact and create two hybrid photonic-plasmonic modes.

#### 4.1.1.    Photonic cavity modes

The designed 1D dielectric heterostructure is a photonic microcavity composed of two DBRs separated by a PU layer, resembling a Fabry-Pérot (FP) cavity. However, unlike a dual-DBR-based FP cavity, the proposed structure is not designed to support a mode at the center of the photonic bandgap (PBG). Instead, the constituent DBRs are designed for a photonic mode at the band-edge to couple to the TP mode. Since the TP modes excited at the DBR–metal interface show a strong

resonance at the band-edge, the photonic mode must be close to the band-edge too. However, an FP cavity with symmetric and identical DBRs on two sides shows photonic modes at the centre of the bandgap. By contrast, an FP cavity with an asymmetrical DBR configuration offers two modes at the lower and higher band-edges. Therefore, the proposed structure has been designed with an asymmetrical arrangement with two different DBRs at two sides of the PU layer to excite a band-edge cavity mode at ~870 nm.

The PBGs of the constituent DBRs control the spectral positions of photonic modes. The refractive indices and thicknesses of the constituent layers of a DBR affect the spectral position of the bandgap, and hence, the resonance wavelength of the excited modes. The center wavelength ($\lambda_c$) of a PBG is given by [47]

$$\lambda_c = 4n_1d_1 = 4n_2d_2, \tag{1}$$

where $n_1$ and $n_2$ are the refractive indices of alternating dielectric layers with thicknesses $d_1$ and $d_2$, respectively. On the other hand, the PBG range varies linearly with the difference of refractive indices of constituent materials.

The photonic microcavity and the two DBRs used to construct it are shown in Fig. 3. $DBR_1$ in Fig. 3(a) is designed to exhibit a PBG from ~840 nm to ~1120 nm, as shown in Fig. 3(b). $DBR_2$ shown in Fig. 3(c) consists of the same materials as $DBR_1$, however, with a different pair number. $DBR_2$ is designed by changing $d_{12}$ in $DBR_1$ to $d_{22}$. DBR arrangements are asymmetric across the PU layer to help couple the photonic mode to TP modes at the metal interface. Therefore, $DBR_2$ must have a PBG that does not overlap with the photonic mode wavelength. Figure 3(d) shows the PBG of $DBR_2$ from ~895 nm to ~1185 nm. Hence, the range of wavelengths from ~845 nm to ~890 nm can propagate through $DBR_2$ to the end.
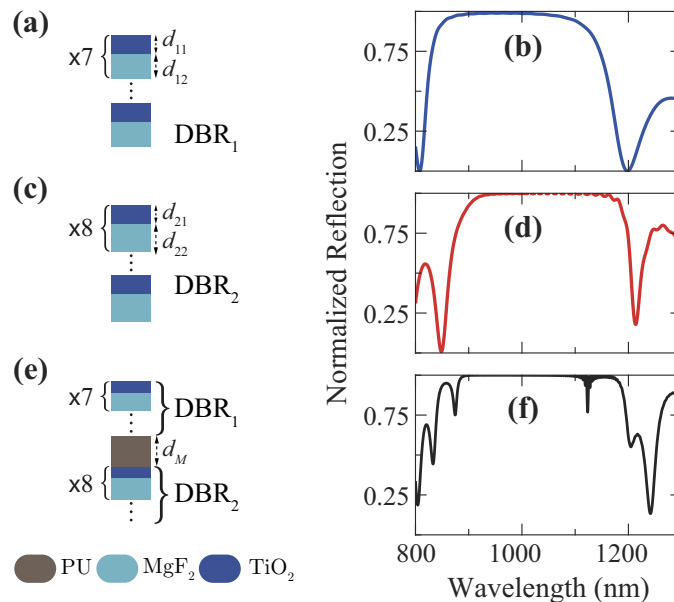


**Fig. 3.** Schematic illustrations of the constituent structures of the proposed laser and their reflection spectra (a,b) $DBR_1$, (c,d) $DBR_2$, and (e,f) $DBR_1$–PU–$DBR_2$.

When $DBR_1$ and $DBR_2$ are combined to form the optical cavity, as shown in Fig. 3(e), the reflection spectra show a PBG from ~845 nm to ~1190 nm, spanning the range of PBGs of both constituent DBRs. The PBG of the combined structure shows two interfacial states at ~877 nm and ~1120 nm, as shown in Fig. 3(f). The mode at ~877 nm falls within the passband of $DBR_2$. These photonic modes at ~877 nm and ~1120 nm arise due to the PU spacer layer, which acts as

a defect in the structure and causes field confinement [20,48]. For $d_M = 325$ nm, the photonic modes are closer to the band-edge at ~870 nm. Band-edge is the site of stronger TP resonance for the proposed laser, offering high-$Q$ modes with better wave localization [32]. Hence, band-edge modes are better than those deep within the bandgap.

### 4.1.2. Plasmonic modes at DBR–metal interface

Since the structure shown in Fig. 3(e) does not have a metal layer, it does not excite plasmonic modes and only supports photonic modes. By contrast, if a 100-nm-thick Au film is incorporated at the bottom of $DBR_2$, with a $TiO_2$ layer in between, TP modes are formed at the $TiO_2$–Au interface. The properties of the isolated photonic and TP modes have been investigated and presented in Fig. 4. The PBG of the DBRs acts as the effective range for tuning both the photonic and plasmonic modes by altering $d_M$ and $d_L$, respectively. On changing $d_M$, the photonic mode shows a redshift across the bandgap, as shown in Fig. 4(a). The $DBR_1$–PU–$DBR_2$–$TiO_2$ configuration has been investigated to analyze the isolated photonic mode. Alongside, the PU–$DBR_2$–$TiO_2$–Au configuration has also been investigated to analyze the isolated TP mode. The PU layer thickness, $d_M$, has been varied for both structures, keeping $d_L$ fixed at 210 nm. The normalized reflection spectra are shown in Figs. 4(a) and 4(b). An increasing $d_M$ redshifts the photonic mode, as shown in Fig. 4(a). Figure 4(b) shows that the change of $d_M$ has a negligible effect on the excited TP mode, and the TP mode remains fixed at ~870 nm. Since the terminal $TiO_2$ layer is not a part of the photonic microcavity, it has a negligible effect on the isolated photonic mode. Hence, when $d_L$ varies with $d_M = 325$ nm, the photonic mode remains fixed at ~877 nm, as shown in Fig. 4(c). However, Fig. 4(d) shows that the TP mode redshifts when $d_L$ increases as the terminal $TiO_2$ layer directly interfaces with the metal.

In this work, the photonic cavity and Tamm plasmon structure are designed to keep the two modes within the IR-140 gain linewidth of ~100 nm centered at lasing wavelength ~870 nm [49]. Therefore, the proposed cavity structure has been designed to modify a typical FP cavity structure by making the DBR arrangement asymmetric and non-identical about the cavity, thus generating stronger intensity in the coupled modes. The optimum $d_M$ and $d_L$ values that create the photonic and plasmonic modes within the gain linewidth are 325 nm and 210 nm, respectively.

### 4.1.3. Hybrid modes in the compound structure

In the proposed structure, the dielectric $DBR_1$–PU–$DBR_2$ optical cavity is connected to the $TiO_2$–Au stack, forming the hybrid dual-mode lasing cavity. The lasing cavity helps couple the photonic and TP modes. Due to the interaction between the photonic and TP modes, two hybrid Tamm modes are manifested as two distinct reflection minima close to the first band-edge of the bandgap for this structure. Figure 5 shows the normalized reflection spectra of the TP structure (devoid of $DBR_1$) and the lasing cavity. The two cases' normalized reflection spectra are compared to understand the structure better. The first case excludes $DBR_1$ from the final structure. Thus, the resulting PU–$DBR_2$–Au structure presented in Fig. 5(a) shows the reflection spectra of Fig. 5(b). A single weak TP mode is observed at the photonic band-edge at ~870 nm. The hybrid cavity composed of $DBR_1$–PU–$DBR_2$–Au is presented in Fig. 5(c), and its reflection spectra are given in Fig. 5(d). The two modes are evident from the reflection spectra of Fig. 5(d).

Compared to the single weak resonance of the first case, the two modes of the second case are highly resonant. Incorporating the $DBR_1$ on top of the PU–$DBR_2$–Au structure adds a new mode to the spectra. These two modes are hybrid Tamm modes, showing stronger resonance than isolated modes and offering dual-mode resonance in the lasing cavity. Since the modes are at the band-edge of the DBR bandgap, they show better confinement and field localization than non-band-edge modes. Also, since the hybrid modes are composed of TPs, the mode volume remains within subwavelength dimensions.
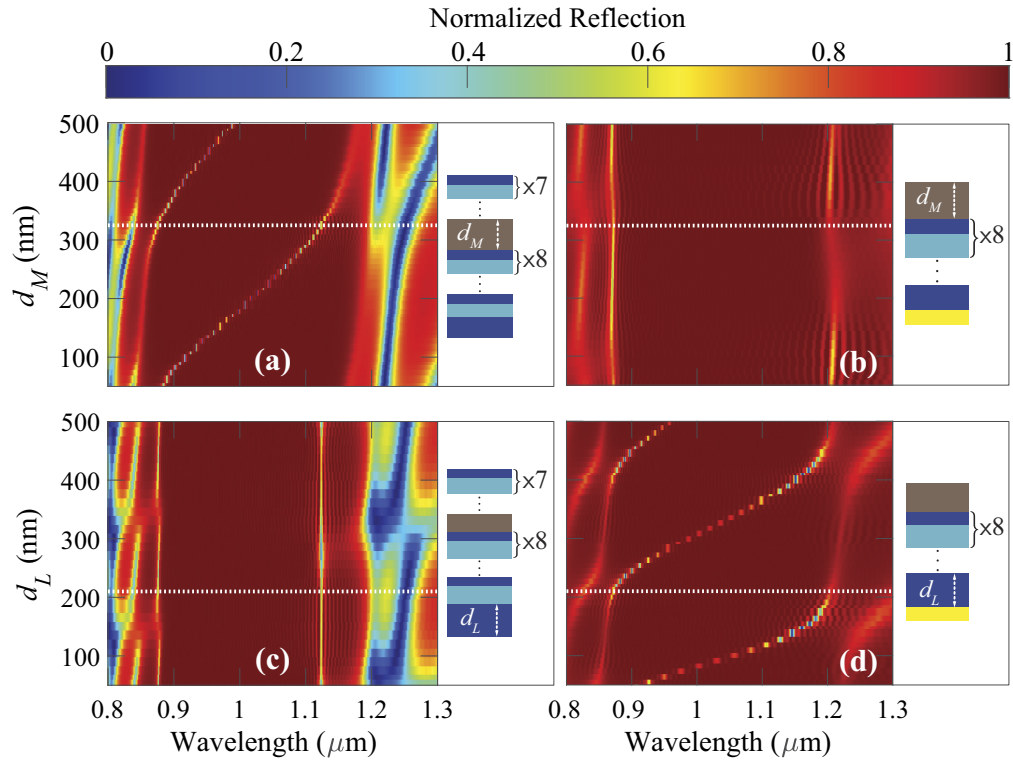
**Fig. 4.** Normalized reflection spectra with the variation of $d_M$ for (a) DBR$_1$–PU–DBR$_2$ and (b) PU–DBR$_2$–Au structures. In both cases, $d_L = 210$ nm. Normalized reflection spectra with the variation of $d_L$ for (c) DBR$_1$–PU–DBR$_2$ and (d) PU–DBR$_2$–Au structures. In both cases, $d_M = 325$ nm.
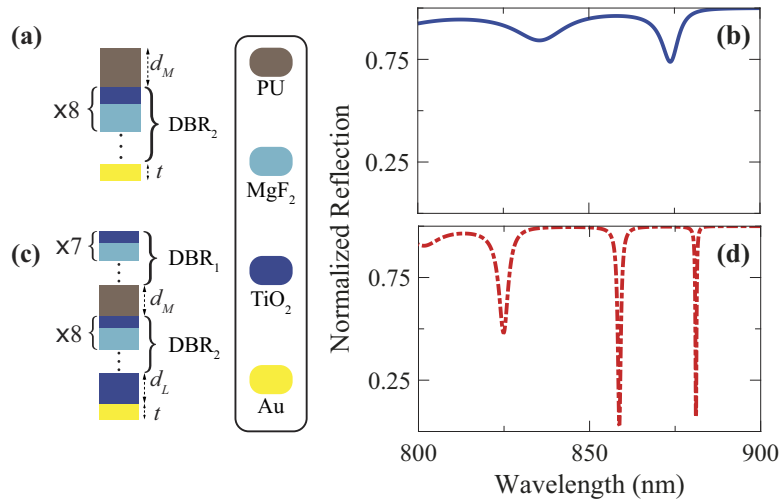


**Fig. 5.** Schematic illustrations and corresponding normalized reflection spectra for (a,b) PU–DBR$_2$–Au structure and (c,d) DBR$_1$–PU–DBR$_2$–Au structure.

The resonance of Fig. 5(d) at 856 nm corresponds to the TP mode at the DBR$_2$–Au interface, while the resonance at 882 nm corresponds to the photonic mode between the two DBRs. Adding the metal layer helps generate the TP mode and make the photonic mode more prominent by making the normalized reflection coefficient more pronounced than Fig. 3(f). Thus, incorporating multiple modes—one between the two DBRs and the other between DBR$_2$ and Au layer—has resulted in two reflection minima and better energy confinement in the proposed structure.

The two hybrid modes show an explicit anti-crossing behavior, which is evidence for the coupling of the photonic and plasmonic modes, as shown in Fig. 6. The isolated modes, indicated by the guiding lines in Fig. 6, show crossing when either $d_L$ or $d_M$ change while keeping the other fixed. The isolated TP mode, independent of $d_M$, is indicated by the vertical white dashed-dotted lines in Figs. 6(a) and (b). The TP line is crossed by the cyan dashed curve of the uncoupled photonic mode in Figs. 6(a) and (b). These uncoupled mode lines are obtained from Figs. 4(a) and (b). The actual hybrid modes of the proposed laser structure deviate from their uncoupled characteristics and avoid crossing, as shown in Fig. 6(b). Similarly, the coupled modes exhibit anti-crossing behavior for varying $d_L$ around ∼210 nm in Figs. 6(c) and (d).
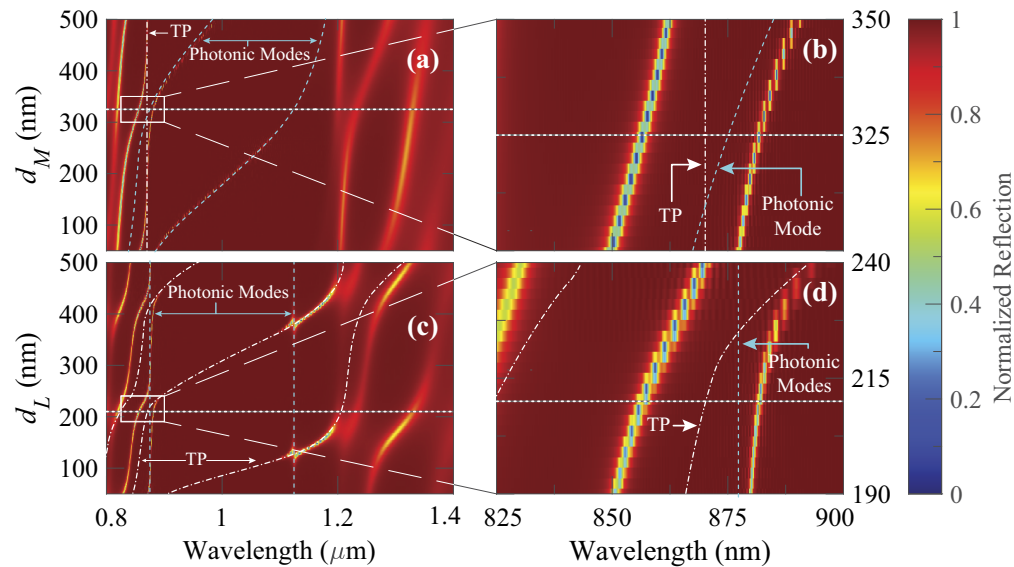


**Fig. 6.** Normalized reflection of DBR$_1$–PU–DBR$_2$–Au structure with the variation of (a,b) $d_M$, when $d_L$ = 210 nm, and (c,d) $d_L$, when $d_M$ = 325 nm. (b,d) show the zoomed-in anti-crossing behaviour. The cyan dashed lines show the uncoupled cavity modes while white dashed-dotted lines show uncoupeld TP modes. The $d_L$ = 210 nm and $d_M$ = 325 nm lines are denoted by white dashed lines.

### 4.1.4.  Extraordinary optical transmission

The electric field intensity within the proposed lasing cavity shows a peak 200-fold enhancement when a solid metal film is used instead of the NHA, as shown in Fig. 7. The electric field concentrates within the cavity at $\lambda_{ps} \approx 856$ nm and $\lambda_{pl} \approx 882$ nm, as exhibited in the intensity profile across the device. For $\lambda_{ps} \approx 856$ nm, the maximum enhancement is ∼90 folds, occurring at the gain region. Furthermore, a ∼200-fold enhancement is observed at the longer wavelength mode in the middle of DBR$_2$.

The plasmons exhibit EOT through the NHA when the holes have subwavelength dimensions [50]. EOT is a different kind of SPP mode excitation in metal with a regular array of subwavelength
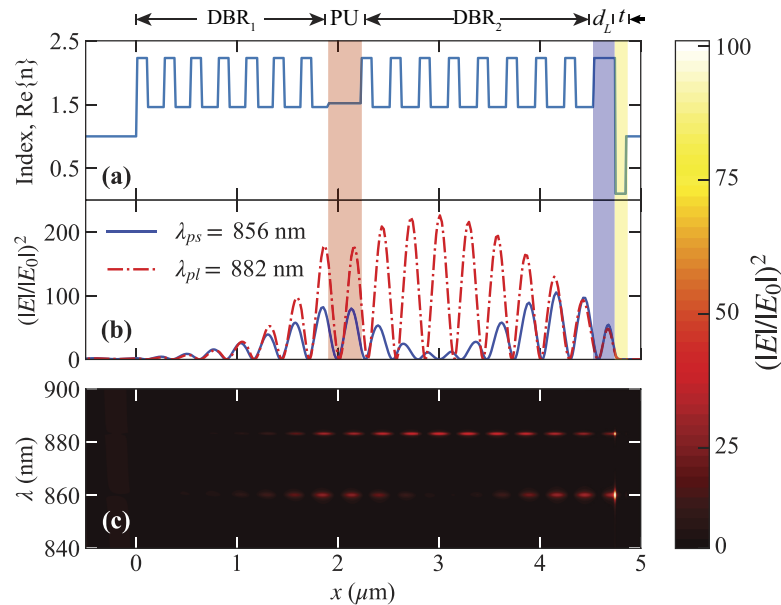
**Fig. 7.** (a) Refractive index profile of the device. (b) $\vec{E}$-field intensity profile in the *x*-direction of the passive lasing cavity, without NHA incorporated in the metal layer. The intensity profile is plotted for $\lambda = 856$ nm (blue line) and $\lambda = 882$ nm (red dashed-dotted line). (c) The $\vec{E}$-field intensity profile in the *x*-direction along the nanohole edge when an NHA is incorporated in the metal layer. The intensity values are normalized to the incident field intensity. The portions of the figures with coloured overlay indicate the following regions: red overlay - gain medium, blue overlay - terminating $TiO_2$ layer, and yellow overlay - Au-film.

holes. The modes excited in EOT are composed of quasi-cylindrical waves at the metal interface along with SPP modes [51]. The plasmonic modes at the hole edges and the metal interface focus energy at hotspots of nanohole edges. The hole dimensions, shape, and array parameters significantly affect the modes. For wavelengths greater than the array period, the NHA transmits more photons than that through the same area of nanoholes without the NHA, resulting in an area-normalized transmission greater than unity. However, the ohmic losses in metal attenuate the transmitted electromagnetic field energy through much of the cross-section of the metal NHA. Therefore, as a transmission device, the performance of a metal NHA can be enhanced by incorporating DBRs, thus validating its application in a laser. DBRs have been cascaded with the metal NHA film in this work to improve the transmission through NHA. The addition of the 1D dielectric photonic crystal to the structure, i.e., the DBR on the metal surface, has experimentally enhanced transmission compared to without the presence of the DBR [39]. This enhancement is attributed to the excitement of TP states at the metal interface [52].

The enhancement due to the NHA patterning is shown in Fig. 7. The inclusion of NHA on the Au layer confines the field significantly at the nanohole edges. The field enhancement is reduced from that observed in an unpatterned metal film in Fig. 7(b) as much as the field is confined at the nanohole edges, resulting in enhanced transmission. Also, as the metal is perforated, the total energy is not reflected from the $DBR_2$–metal interface. However, in Fig. 7(c), the increased intensity of electric-field at selected wavelengths within the cavity shows that the feedback provided by the cavity is significant. The maximum intensity is in the central region around the gain medium. The plasmonic cavity traps stimulating energy within the structure's gain medium and paves the way for the emission of dual-mode lasing.

### 4.1.5.  Spatial field distribution

The electric field distribution throughout the structure presented in Fig. 8 shows various spatial modes. The physics behind lasing of the proposed structure can be further analyzed from the field profiles at different cross-sections of the structures. In Fig. 8, the fields at the nanohole edges show enhancement. The hotspots at the nanohole edges show 80-fold and 50-fold enhancement of the electric field intensity for the two resonant modes. The intensity enhancement demonstrates the strong coupling of photonic and TP modes. It has been possible to identify the coupled resonant modes by observing the spatial $\vec{E}$-field distribution.
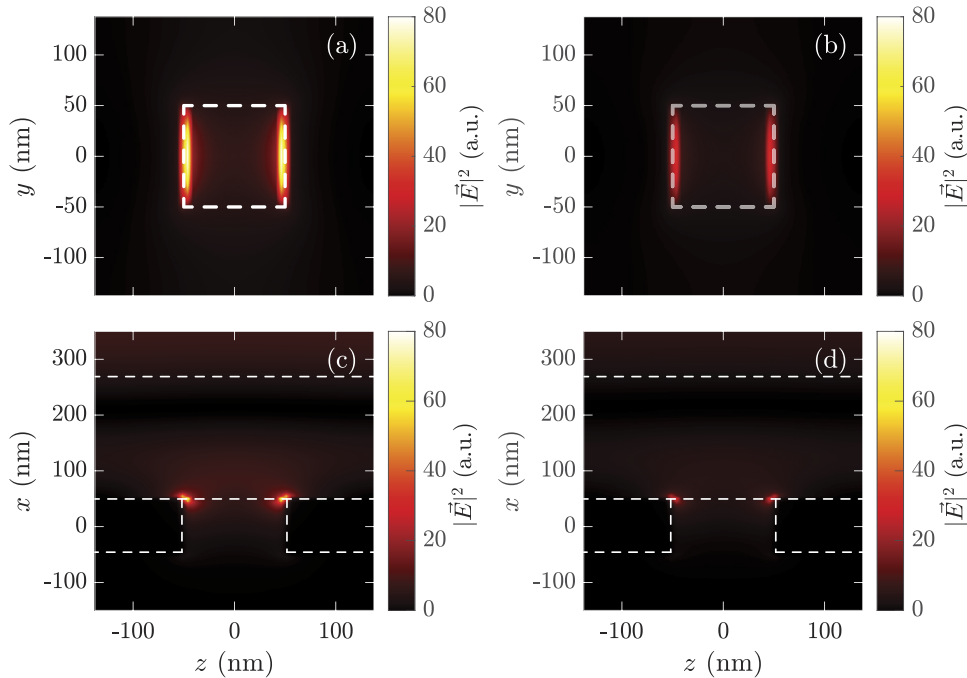


**Fig. 8.** (a)-(b): The transverse section $\vec{E}$-field intensity profile of the proposed structure taken along the metal-terminating $TiO_2$ layer interface.(c)-(d) The longitudinal section $\vec{E}$-field intensity profile of the proposed structure taken along the dashed line shown along $y = 0$ of the figure (a),(b). (a),(c) Shorter wavelength $|\vec{E}|^2$ intensity profile at 856 nm. (b),(d) Longer wavelength $|\vec{E}|^2$ intensity profile at 882 nm.

### 4.2.  Dual mode lasing emission

Now, IR-140 dye molecules are included in the PU-based gain medium of the laser to get the lasing response. Figure 9(a) shows that the device emits two distinct lasing modes at ~865 nm and ~885 nm with a 20-nm separation between them. Figure 9(a) also indicates that the $DBR_1$–gain medium–$DBR_2$ structure emits only a single-mode (red dashed-dotted curve) at ~875 nm without the Au NHA. However, incorporating a metal NHA attenuates the emission intensity due to the loss associated with the plasmonic mode. Notably, the $DBR_1$–gain–Au-NHA structure, similar to the structure reported by Ref. [53], also exhibits a single mode. By contrast, the proposed laser emits dual modes when two DBRs are used. Figure 9(b) shows the effect of changing pump input energy on output spectral intensity for two pump energies. The proposed laser's pump input versus output emission characteristics show threshold behavior, as shown in Fig. 9(c). The output emission occurs abruptly once the input pump overcomes the threshold

required for lasing emission—an inherent feature for lasers [54]. Pump intensity thresholds exist at 10.02 $\mu$J/cm$^2$ for the smaller wavelength mode and 12.95 $\mu$J/cm$^2$ for the longer wavelength lasing mode, which are much smaller than the thresholds of similar dual-wavelength plasmonic lasers reported recently [33,34]. Both the peaks of dual-mode lasing at around 865 nm and 885 nm wavelengths show a rising trend with the input pump amplitude. Both the peaks show almost equal emission intensity for pump intensity $\gtrsim$160 $\mu$J/cm$^2$.
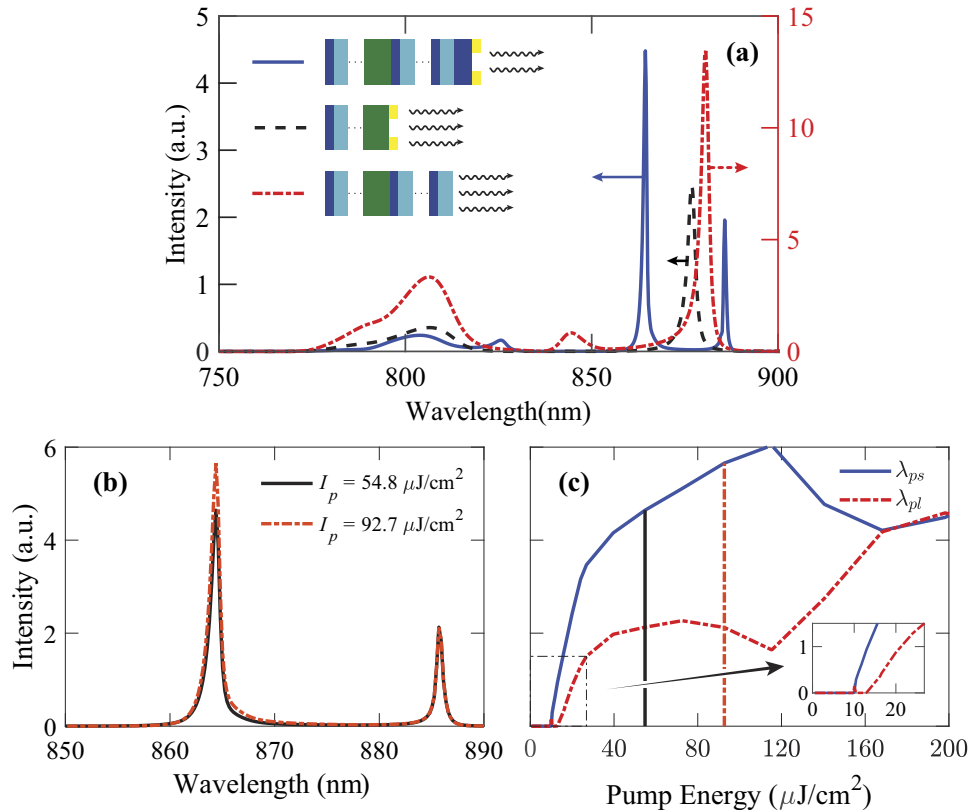


**Fig. 9.** (a) Lasing emission spectra of the proposed laser structure (blue curve), a structure akin to the one reported by Ref. [53] with hole width and periodicity changed to $d_h$ and $\Lambda$, respectively (black dashed curve), and the laser structure without the metal film (red-dashed-dotted curve). (b) Dual-mode lasing emission of the proposed laser structure for two pump intensities. (c) Peak intensity for the two modes versus the pump energy.

Although the proposed laser creates dual lasing modes using hybrid Tamm modes, more than two lasing modes can be obtained in principle. Additional photonic modes can be excited from cavity engineering and hybridized with the TP mode to generate more than two hybrid modes. However, the resonances must be within the limited ~100 nm gain linewidth of the IR-140 dye molecules, and the cavity engineering may add complexity to the structure. The number of modes will also be limited by the additional requirement of gain or pumping.

### 4.2.1. Near-field mode dynamics

The spectral characteristics of the lasing modes are dependent on some of the laser cavity parameters. In this work, the number of alternating pairs in both DBRs, $N_1$ and $N_2$, and the thicknesses $d_L$ and $d_M$ are varied to investigate the change in the lasing spectra.

**Tuning $N_1$ and $N_2$:**  The effects of varying the pair number in each DBR are different. Figure 10(a) shows that when $N_1$ increases, it refines the existing resonant modes by decreasing the emission linewidth. The increasing $N_1$ also increases the emission by reflecting it away from the input side toward the output side, causing amplification and narrowing lasing modes. The spectral positions of the modes remain unaffected due to the variation of $N_1$. By contrast, $N_2$ affects the spectral positions of the modes, as shown in Fig. 10(b). The lasing modes redshift in the range from 850 nm to 890 nm when $N_2$ increases, exhibiting a maximum gain at 870 nm.
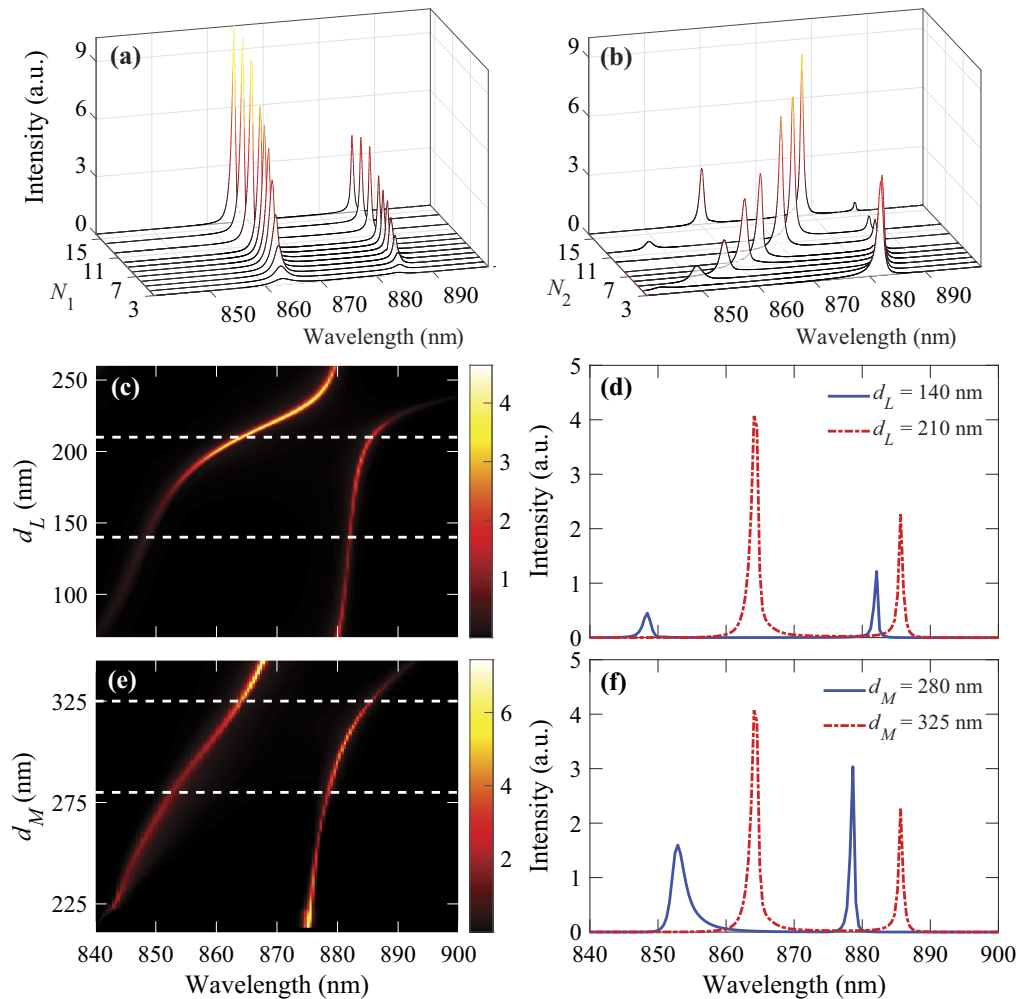


**Fig. 10.** (a) Emission intensity spectrum for varying the number of $TiO_2/MgF_2$ pairs in (a) DBR$_1$ ($N_1$) and (b) DBR$_2$ ($N_2$). (c) Lasing emission intensity spectra for varying $d_L$. (d) Lasing spectra for $d_L$ = 140 nm and 210 nm, as indicated in (c) by the white dashed lines. (e) Lasing emission intensity spectra for varying $d_M$. (f) Lasing spectra for $d_M$ = 280 nm and 325 nm, as indicated in (e) by the white dashed lines.

**Tuning terminating $TiO_2$ layer:**  The change of $d_L$ linearly varies the resonant wavelength within the PBG of the DBR, as expected for TP resonance [55]. As per the results presented in Ref. [55], the TP resonance within the PBG shifts to longer wavelengths when $d_L$ increases until it crosses the longer wavelength, i.e., the upper band-edge of the PBG. Once the upper

band-edge is crossed, TP modes reappear at the smaller wavelength, i.e., the lower band-edge of the PBG, except that the TP resonances are more closely spaced in this case. Thus, with increasing $d_L$, the smaller wavelength lasing modes shift to the longer wavelengths along the PBG in the spectrum, as shown in Fig. 10(c,d). However, the redshift of the shorter wavelength mode is more prominent than the longer wavelength mode, verifying that the shorter wavelength mode is the TP mode, generated at the metal–terminating $TiO_2$ interface. It has been shown that the variation of the layer just preceding the metal NHA shifts the resonant modes along the PBG.

**Tuning gain medium thickness:** The variation in $d_M$ also tunes the spectral position of the modes, as presented in Fig. 10(e,f). The emission peak redshifts with increasing $d_M$. However, for $d_M \lesssim 220$ nm and $\gtrsim 330$ nm, the spectra show only a single-mode emission because of the limited gain lineshape centering 870 nm and the PBG of the DBR.

### 4.2.2. Far-field analysis

Plasmonic lasers emit higher-order modes and lack directionality in the spatial domain if not appropriately designed. The difference between the wavevectors of the free-space propagating modes and the surface plasmon modes is the origin of the higher-order spatial modes. The higher-order modes can be suppressed if the NHA has a periodicity within the subwavelength range. Thus, ensuring subwavelength periodicity of the NHA, the proposed laser emits only zeroth order mode. This work simulates an area of 150 $\mu$m $\times$ 150 $\mu$m along the $yz$-plane of the device to get the far-field beam distribution. The far-fields for both modes have been analyzed separately and similar results have been found. The far-field profiles are given in Fig. 11. The nanoholes act as hotspptots for resonant modes and secondary point sources for the far-field. The emissions from the secondary sources interfere in the far-field to create an interference pattern on the hemisphere 1 m away, having Gaussian distribution. Figure 11 shows that the far-field emission intensity is confined within 0.35° polar angle at 1m distance from the near-field.
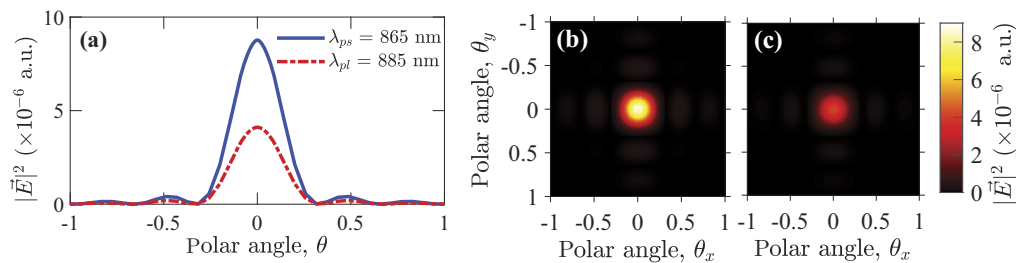


**Fig. 11.** (a) Electric field intensity distribution at the far-field with respect to polar angle ($\theta$) at 0° azimuth. Polar 2D spatial farfield intensity for (b) $\lambda_{ps} = 865$ nm and (c) $\lambda_{pl} = 885$ nm.

## 5. Conclusion

In conclusion, this work theoretically demonstrates dual-mode emission from a hybrid Tamm plasmonic laser. The dual-mode emission is created by hybridizing the plasmonic and photonic modes. While the two cascaded DBRs create photonic modes with a gain medium between them, the interface between the second DBR and metal layer excites the plasmonic mode. The hybridized modes created from the interaction of the photonic and plasmonic modes fall within the linewidth of the IR-140-doped PU gain medium and result in dual-mode lasing. The emission spectra can be tuned by varying the DBR pair numbers and the thicknesses of the PU gain layer and $TiO_2$ dielectric layer interfacing with the metal NHA. Furthermore, the higher-order spatial modes in the far-field emission pattern, a well-known drawback of plasmonic lasers, have been

suppressed using subwavelength periodicity in the metal NHA, limiting the emission only to the zeroth-order mode.

**Disclosures.** The authors declare no conflicts of interest.

**Data availability.** Data underlying the results presented in this paper are not publicly available at this time but may be obtained from the authors upon reasonable request.

## References

1. R. Zia, J. A. Schuller, A. Chandran, and M. L. Brongersma, "Plasmonics: the next chip-scale technology," Mater. Today **9**(7-8), 20–27 (2006).
2. U. Koch, C. Uhl, and H. Hettrich, *et al.*, "A monolithic bipolar CMOS electronic–plasmonic high-speed transmitter," Nat. Electron. **3**(6), 338–345 (2020).
3. N. Pleros, E. E. Kriezis, and K. Vyrsokinos, "Optical interconnects using plasmonics and si-photonics," IEEE Photonics J. **3**(2), 296–301 (2011).
4. B. M. Walsh, "Dual wavelength lasers," Laser Phys. **20**(3), 622–634 (2010).
5. L. Sánchez-García, M. O. Ramirez, R. M. Solé, J. J. Carvajal, F. Díaz, and L. E. Bausá, "Plasmon-induced dual-wavelength operation in a Yb3+ laser," Light: Sci. Appl. **8**(1), 14 (2019).
6. G. David, A. Miffre, B. Thomas, and P. Rairoux, "Sensitive and accurate dual-wavelength uv-vis polarization detector for optical remote sensing of tropospheric aerosols," Appl. Phys. B **108**(1), 197–216 (2012).
7. I. Park, C. Sydlo, I. Fischer, W. Elsäßer, and H. Hartnagel, "Generation and spectroscopic application of tunable continuous-wave terahertz radiation using a dual-mode semiconductor laser," Meas. Sci. Technol. **19**(6), 065305 (2008).
8. D. Ozcelik, J. W. Parks, T. A. Wall, M. A. Stott, H. Cai, J. W. Parks, A. R. Hawkins, and H. Schmidt, "Optofluidic wavelength division multiplexing for single-virus detection," Proc. Natl. Acad. Sci. **112**(42), 12933–12937 (2015).
9. K. Koo and A. Kersey, "Bragg grating-based laser sensors systems with interferometric interrogation and wavelength division multiplexing," J. Lightwave Technol. **13**(7), 1243–1249 (1995).
10. K. Meiners-Hagen, R. Schödel, F. Pollinger, and A. Abou-Zeid, "Multi-wavelength interferometry for length measurements using diode lasers," Meas. Sci. Rev. **9**(1), 16–26 (2009).
11. R. Dändliker, R. Thalmann, and D. Prongué, "Two-wavelength laser interferometry using superheterodyne detection," Opt. Lett. **13**(5), 339–341 (1988).
12. M. T. Hill, Y.-S. Oei, B. Smalbrugge, Y. Zhu, T. De Vries, P. J. Van Veldhoven, F. W. Van Otten, T. J. Eijkemans, J. P. Turkiewicz, H. De Waardt, E. J. Geluk, S.-H. Kwon, Y.-H. Lee, R. Nötzel, and M. K. Smit, "Lasing in metallic-coated nanocavities," Nat. Photonics **1**(10), 589–594 (2007).
13. A. V. Maslov and C. Z. Ning, "Size reduction of a semiconductor nanowire laser by using metal coating," in *Physics and Simulation of Optoelectronic Devices XV*, vol. 6468 M. Osinski, F. Henneberger, and Y. Arakawa, eds., International Society for Optics and Photonics (SPIE, 2007), pp. 138–144.
14. D. J. Bergman and M. I. Stockman, "Surface plasmon amplification by stimulated emission of radiation: quantum generation of coherent surface plasmons in nanosystems," Phys. Rev. Lett. **90**(2), 027402 (2003).
15. M. I. Stockman, "Spasers explained," Nat. Photonics **2**(6), 327–329 (2008).
16. N. I. Zheludev, S. L. Prosvirnin, N. Papasimakis, and V. A. Fedotov, "Lasing spaser," Nat. Photonics **2**(6), 351–354 (2008).
17. J. Y. Suh, C. H. Kim, W. Zhou, M. D. Huntington, D. T. Co, M. R. Wasielewski, and T. W. Odom, "Plasmonic Bowtie Nanolaser Arrays," Nano Lett. **12**(11), 5769–5774 (2012).
18. W. Zhou, M. Dridi, J. Y. Suh, C. H. Kim, D. T. Co, M. R. Wasielewski, G. C. Schatz, and T. W. Odom, "Lasing action in strongly coupled plasmonic nanocavity arrays," Nat. Nanotechnol. **8**(7), 506–511 (2013).
19. Z. Azad and M. A. Talukder, "Simultaneously surface- and edge-emitting plasmonic laser operating in the near-infrared region," Opt. Laser Technol. **146**, 107571 (2022).
20. Y. Akahane, T. Asano, B.-S. Song, and S. Noda, "High-Q photonic nanocavity in a two-dimensional photonic crystal," Nature **425**(6961), 944–947 (2003).
21. X. Yang, A. Ishikawa, X. Yin, and X. Zhang, "Hybrid Photonic-Plasmonic Crystal Nanocavities," ACS Nano **5**(4), 2831–2838 (2011).
22. B. Wang, P. Yu, W. Wang, X. Zhang, H. Kuo, H. Xu, and Z. M. Wang, "High-Q Plasmonic Resonances: Fundamentals and Applications," Adv. Opt. Mater. **9**(7), 2001520 (2021).
23. M. Kaliteevski, I. Iorsh, S. Brand, R. Abram, J. Chamberlain, A. Kavokin, and I. Shelykh, "Tamm plasmon-polaritons: Possible electromagnetic states at the interface of a metal and a dielectric bragg mirror," Phys. Rev. B **76**(16), 165415 (2007).
24. M. Sasin, R. Seisyan, M. Kalitteevski, S. Brand, R. Abram, J. Chamberlain, A. Y. Egorov, A. Vasil'Ev, V. Mikhrin, and A. Kavokin, "Tamm plasmon polaritons: Slow and spatially compact light," Appl. Phys. Lett. **92**(25), 251112 (2008).
25. R. Brückner, M. Sudzius, S. Hintschich, H. Fröb, V. Lyssenko, and K. Leo, "Hybrid optical tamm states in a planar dielectric microcavity," Phys. Rev. B **83**(3), 033405 (2011).
26. S. Chen, "Dual-mode near-infrared light tunable absorber based on graphene by optical tamm state and microcavity," Opt. Commun. **492**, 126962 (2021).

27. R. V. Nair, "The interaction between optical tamm state and microcavity mode in a planar hybrid plasmonic-photonic structure," Photonics Nanostructures-Fundamentals Appl. **36**, 100702 (2019).

28. S. S.-U. Rahman, T. Klein, S. Klembt, J. Gutowski, D. Hommel, and K. Sebald, "Observation of a hybrid state of Tamm plasmons and microcavity exciton polaritons," Sci. Rep. **6**(1), 34392 (2016).

29. M. Kaliteevski, S. Brand, R. Abram, I. Iorsh, A. Kavokin, and I. Shelykh, "Hybrid states of tamm plasmons and exciton polaritons," Appl. Phys. Lett. **95**(25), 251108 (2009).

30. B. Afinogenov, V. Bessonov, A. Nikulin, and A. Fedyanin, "Observation of hybrid state of tamm and surface plasmon-polaritons in one-dimensional photonic crystals," Appl. Phys. Lett. **103**(6), 061112 (2013).

31. H. Liu, J. Gao, Z. Liu, X. Wang, H. Yang, and H. Chen, "Large electromagnetic field enhancement achieved through coupling localized surface plasmons to hybrid tamm plasmons," J. Opt. Soc. Am. B **32**(10), 2061–2067 (2015).

32. D. Wang, A. Yang, W. Wang, Y. Hua, R. D. Schaller, G. C. Schatz, and T. W. Odom, "Band-edge engineering for controlled multi-modal nanolasing in plasmonic superlattices," Nat. Nanotechnol. **12**(9), 889–894 (2017).

33. S. Pourjamal, T. K. Hakala, M. Nečada, F. Freire-Fernández, M. Kataja, H. Rekola, J.-P. Martikainen, P. Törmä, and S. van Dijken, "Lasing in ni nanodisk arrays," ACS Nano **13**(5), 5686–5692 (2019).

34. J. M. Winkler, M. J. Ruckriegel, H. Rojo, R. C. Keitel, E. De Leo, F. T. Rabouw, and D. J. Norris, "Dual-wavelength lasing in quantum-dot plasmonic lattice lasers," ACS Nano **14**(5), 5223–5232 (2020).

35. S. Shahid, S.-E. Zumrat, and M. A. Talukder, "A merged lattice metal nanohole array based dual-mode plasmonic laser with an ultra-low threshold," Nanoscale Adv. **4**(3), 801–813 (2022).

36. Y. Liu, Q. Tang, L. Zhang, X. La, L. Zhao, W. Wang, and S. Liang, "Dual-wavelength DBR laser integrated with high-speed EAM for THz communications," Opt. Express **28**(7), 10542–10551 (2020).

37. C. Symonds, S. Azzini, G. Lheureux, A. Piednoir, J. M. Benoit, A. Lemaitre, P. Senellart, and J. Bellessa, "High quality factor confined Tamm modes," Sci. Rep. **7**(1), 3859 (2017).

38. P. B. Johnson and R.-W. Christy, "Optical constants of the noble metals," Phys. Rev. B **6**(12), 4370–4379 (1972).

39. P. N. Melentiev, A. E. Afanasiev, A. A. Kuzin, A. V. Zablotskiy, A. S. Baturin, and V. I. Balykin, "Single nanohole and photonic crystal: wavelength selective enhanced transmission of light," Opt. Express **19**(23), 22743 (2011).

40. A. Taflove and S. C. Hagness, *Computational electrodynamics: the finite-difference time-domain method* (Artech house, 2005).

41. Lumerical Inc, "FDTD: 3D electromagnetic simulator," https://www.lumerical.com/products/fdtd/ (2020). Accessed: 2022-05-19.

42. M. Dridi and G. C. Schatz, "Model for describing plasmon-enhanced lasers that combines rate equations with finite-difference time-domain," J. Opt. Soc. Am. B **30**(11), 2791 (2013).

43. S.-H. Chang and A. Taflove, "Finite-difference time-domain model of lasing action in a four-level two-electron atomic system," Opt. Express **12**(16), 3827–3833 (2004).

44. A. Yang, T. B. Hoang, M. Dridi, C. Deeb, M. H. Mikkelsen, G. C. Schatz, and T. W. Odom, "Real-time tunable lasing from plasmonic nanocavity arrays," Nat. Commun. **6**(1), 6939 (2015).

45. J. A. Schuller, E. S. Barnard, W. Cai, Y. C. Jun, J. S. White, and M. L. Brongersma, "Plasmonics for extreme light concentration and manipulation," Nat. Mater. **9**(3), 193–204 (2010).

46. M. Noginov, G. Zhu, A. Belgrave, R. Bakker, V. Shalaev, E. Narimanov, S. Stout, E. Herz, T. Suteewong, and U. Wiesner, "Demonstration of a spaser-based nanolaser," Nature **460**(7259), 1110–1112 (2009).

47. W. Yu, L. Shen, Y. Long, P. Shen, W. Guo, W. Chen, and S. Ruan, "Highly efficient and high transmittance semitransparent polymer solar cells with one-dimensional photonic crystals as distributed bragg reflectors," Org. Electron. **15**(2), 470–477 (2014).

48. A. Kavokin, I. Shelykh, and G. Malpuech, "Lossless interface modes at the boundary between two periodic dielectric structures," Phys. Rev. B **72**(23), 233102 (2005).

49. Z. Azad, M. S. Islam, and M. A. Talukder, "Mode-resolved analysis of a planar multi-layer plasmonic nanolaser," Opt. Commun. **482**, 126614 (2021).

50. T. W. Ebbesen, H. J. Lezec, H. Ghaemi, T. Thio, and P. A. Wolff, "Extraordinary optical transmission through sub-wavelength hole arrays," Nature **391**(6668), 667–669 (1998).

51. H. Liu and P. Lalanne, "Microscopic theory of the extraordinary optical transmission," Nature **452**(7188), 728–731 (2008).

52. I. V. Treshin, V. V. Klimov, P. N. Melentiev, and V. I. Balykin, "Optical Tamm state and extraordinary light transmission through a nanoaperture," Phys. Rev. A **88**(2), 023832 (2013).

53. Z. Ahmed and M. A. Talukder, "An efficient and directional optical tamm state assisted plasmonic nanolaser with broad tuning range," J. Phys. Commun. **2**(4), 045016 (2018).

54. G. Björk, A. Karlsson, and Y. Yamamoto, "Definition of a laser threshold," Phys. Rev. A **50**(2), 1675–1680 (1994).

55. H. Zhou, G. Yang, K. Wang, H. Long, and P. Lu, "Multiple optical tamm states at a metal–dielectric mirror interface," Opt. Lett. **35**(24), 4112–4114 (2010).